

# Synchrotron X-ray imaging study on the mechanism of solids transfer to bitumen froth during oil sands flotation 1: True flotation

Hanyu Zhang<sup>a</sup>, Liuyin Xia<sup>a\*</sup>, Ning Zhu<sup>b</sup>, Sergey Gasilov<sup>b</sup>, Iris He<sup>a</sup>, Xiaofan Ding<sup>b</sup>

<sup>a</sup> Department of Chemical and Materials Engineering, University of Alberta, Edmonton, AB, Canada, T6G 2R3

<sup>b</sup> Canadian Light Source Inc., 44 Innovation Blvd, Saskatoon, SK, Canada, S7N 2V3

## Abstract

The extraction of bitumen from oil sands using the water-based method was conducted at 50°C, 30% pulp density and pH 8.5. The collected bitumen froth was immediately characterized using X-ray imaging in micro-computed tomography mode (micro-CT). Synchrotron-based technology, with a photon flux  $10^6$  higher than lab-based X-ray systems, allowed for a CT scan with a voxel size of 6.5  $\mu\text{m}$  to be completed in 0.1 seconds. This enables imaging of freshly prepared bitumen froth without any special arrangements, such as freezing. Image processing and segmentation included the removal of ring-shaped artifacts, differentiation of sand and non-sand particles, building a 3D model for quantitative analysis, and identification of mineral particles attached to air bubbles. This research provided visualization of more than 14,000 unwanted solids transported to bitumen froth. It offers direct evidence of the distribution and association of particles in the bitumen froth. It was observed that some particles were carried to the froth layer through true

---

\* Corresponding author.  
E-mail address: [liuyin@ualberta.ca](mailto:liuyin@ualberta.ca) (L. Xia)

20 flotation, and those particles not attached to air bubbles had a significantly smaller size, which  
21 cannot be revealed by traditional off-site analysis methods.

22 **Keywords:** Bitumen froth, Solids, Synchrotron radiation, X-ray micro-computed tomography  
23 (micro-CT), True flotation, Entrainment

24

## 1. Introduction

Oil sands, the most abundant energy resource in Canada, are a crucial component of global energy security due to their significant contribution to crude oil supply [1, 2]. In 2023, Canadian exports of crude oil reached a record high, totalled 230.0 million cubic metres crude oil [3]. The industrial (commercialized) bitumen concentration method for surface mined oil sands ore is water-based extraction process, which is essential the froth flotation separating bitumen from sands [4]. The bitumen froth product typically contains 50-60 wt.% bitumen, 30-40 wt.% water, and 10-15 wt.% solids [5, 6]. The solids content in a poor-quality bitumen froth would even higher. The unwanted mineral solids within bitumen froth lead to greater solvent usage and higher hydrocarbon loss in downstream processing [7], thereby impacting the cost-effectiveness and efficiency of synthetic crude oil (SCO) production.

Oil sands companies are striving to produce higher quality bitumen froth with fewer solids. There is a knowledge gap for uncovering reasons behind the presence of mineral solids in bitumen froth during the water-based extraction process. Solid particles are believed to report to the froth layer during flotation through complex mechanisms, including true flotation, mechanical entrainment, slime coating, and unliberated or coagulated bitumen-solid aggregates [8]. The carryover of unwanted solids with bitumen flotation is more complex, which related to the new knowledge of interaction between air bubbles, water, bitumen drops and mineral solids during water-based extraction. To the best of our knowledge, existing studies typically rely on indirect analysis methods [9], such as Dean Stark method, which involves washing out solids for solids content analysis, along with off-site particle size distribution and mineralogical analysis. No published research has directly revealed the distribution and association of mineral solids in bitumen froth. Characterization that provides sufficient spatial information for studying the mechanisms of

mineral solids carryover to froth is still lack, particularly regarding the aggregation of multiple particles and air bubbles.

Optical imaging techniques have been frequently employed to observe bubbles and particles distributions and associations in froth flotation [10]. Trajectories of air bubbles and bubble-particles are tracked, and usually optical imaging techniques can reveal the attachment and detachment of mineral particles and air bubbles. However, the opaque nature of bitumen froth precludes direct observation and tracking of particles in this system. Similarly, optical-based techniques such as high-speed photography particle tracking velocimetry [11], laser doppler velocimetry [12], particle image velocimetry [13], and particle shadow velocimetry [14], are not applicable for analyzing bitumen froth.

Recent advancements in X-ray micro-computed tomography (micro-CT) have enabled detailed 3D imaging of bubble clusters, revealing mineral attachment to air bubbles with high resolution and distinguishing minerals based on density differences [15-17]. However, conventional micro-CT requires several hours to complete a full scan to ensure image quality and sample details. For example, Anzoom et al. [17] acquired 2880 projects with a scan duration of 1.5 hours. In the dynamic environment of bitumen froth where bubbles continuously move, breakup, and coalescence, maintaining stability for extended micro-CT scan is impractical. Anzoom et al. [17] addressed this by freezing bubble clusters using a customized arrangement, effectively keeping the agglomerates in a fixed position during the scan, despite freezing can influence the shape and position of the bubbles. Micro-CT also has been widely used in petrology, mineralogy, and geometallurgy for sample analysis and characterization as a non-destructive testing method, including determination of microstructure [18], quantitative characterization of pore size distributions and morphology [19], and analysis of mineral grade and distribution and mineral

association [20]. For the complex bitumen froth system, including mineral solids, bitumen and water, and air bubbles, micro-CT could provide superior analysis and projection of the froth internal features, visualizing the mineral solids distribution and their association to air bubbles. Despite its potential, X-ray imaging of real flotation froth has not yet been explored. Synchrotron-based X-ray imaging, with a photon flux  $10^6$  higher than lab-based X-ray systems, offers high temporal resolution and spatial resolution [21]. This advanced technique is tailored to the nature of bitumen froth. It has been utilized recently in pore studies, the analysis of bubble formation and drainage with foam [22, 23]. The objective of this study is to employ synchrotron X-ray micro-computed tomography to reveal the internal microstructure of bitumen froth. It aims to visualize and analyze the distribution of sands and heavy mineral solids, and their association with air bubbles.

## 2. Methodology

### 2.1 Bitumen froth preparation

The oil sands ore sample used in this work was collected from a mining site situated in Athabasca region located in northern Alberta, Canada. A Denver D-12 flotation machine was used to conduct froth flotation to collect bitumen froth from the ore. The flotation parameters were set at 30% pulp density, 1000 rpm, 3 L/min air flowrate, pH 8.5 and the collection of bitumen froth was executed at 50°C. The aerated froth was collected promptly at the beginning of the flotation, and then immediately transferred into a cylindrical container with a 10 mm diameter and approximately 4-5 mm in height. This immediate transfer and the use of shallow container were essential to preserve the integrity and freshness of the bitumen froth. Subsequently, these fresh prepared samples were subjected to synchrotron-based micro-CT scanning.

### 2.2 Image acquisition

The high-resolution X-ray imaging of bitumen froth was conducted at the 05ID-2 beamline of the BioMedical Imaging and Therapy (BMIT) facility at the Canadian Light Source (CLS). The 05ID-2 beamline provided a monochromatic X-ray with photon energy of 60 keV for CT scans. The bitumen froth sample in the sample container was put in the SOE-1 experimental hutch [24] for X-ray imaging acquisition. In order to improve the contrast to better distinguish the components in bitumen froth, a phase-sensitive imaging method, propagation-based imaging (PBI, also called in-line phase contrast imaging), was applied. Propagation distance (i.e., the distance between the sample and the detector) is the crucial factor to determine the resulting image contrast in PBI [25]. In this batch of testing, after several trials to find the optimal position, the propagation distance was determined to be 0.6 m. The X-ray detector (AA60 beam monitor (Hamamatsu, Japan) with the sCMOS camera of PCO Edge 5.5) used in this work provided a pixel size of 6.5  $\mu\text{m}$ . The

exposure time per projection was 50 ms. A typical CT scan with 2000 projections captured in  $180^\circ$  took less than 3 min. This rapid and detailed imaging provided crucial volumetric data for analyzing the internal microstructure of the bitumen froth.

### 2.3 Image processing

An image processing toolkit developed based on the open source *ufo framework*, *tofu ez* [26], was used to reconstruct images after the CT data acquisition. As shown in Figure 1(a), the reconstructed images had ring artifacts that were semi-circular and ring-shaped artifacts on projection. It is caused by small errors in detector pixel values to persist throughout CT acquisition. The existence of ring artifact will impact subsequent segmentation. To remove ring artifacts in these images, we used a Matlab application developed by Wei and coworkers [27]. The removal starts by transforming the images into polar coordinates, and then the polar image is decomposed into four image components using a 2D wavelet transform: the low-pass band image component, and the components from horizontal, vertical, and diagonal details bands. A 2D Fourier transform is applied to the vertical details band image component only, as the ring artifacts become vertical lines in the polar coordinates. Gaussian filtering [28] is then applied in the Fourier domain along the abscissa direction to suppress the vertical lines. After above processing, inverse Fourier transform followed by inverse wavelet transform are performed to get the corrected polar image. The corrected polar image is then converted back to Cartesian coordinates to produce an image with reduced artifacts. Figure 1(b) shows the reconstructed image after ring artifacts removal. In addition, the bright dots in the enlarged image in Figure 1(b) indicates that the objects there have a higher density. In oil sands, these particles should be heavy minerals, such as rutile ( $\text{TiO}_2$ ) and zircon ( $\text{ZrO}_2$ ). We refer to these bright particles as non-sand minerals. The irregular areas with

medium gray values are the most common solid components in oil sand, such as quartz and clay, which we call sands. The structures that are relatively circular with lower gray values are bubbles.

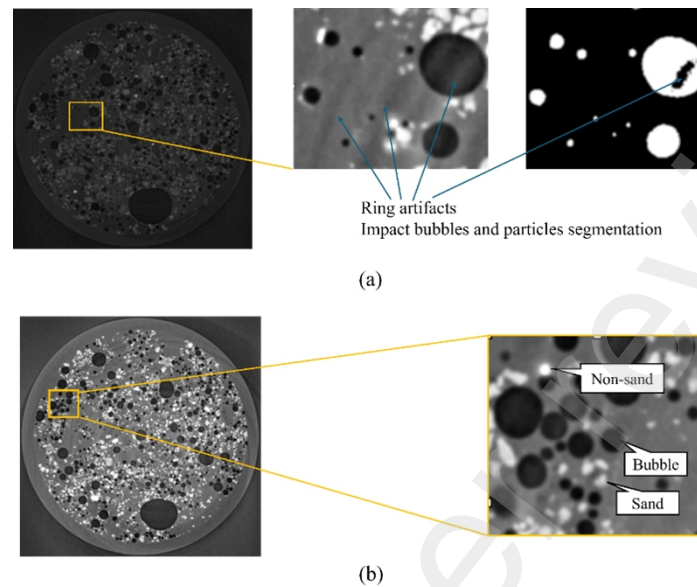


Figure 1. Diagram of a reconstructed slice (a) before ring artifacts removal, and (b) after ring artifacts removal.

## 2.4 Image segmentation

ImageJ was used to segment particles and air bubbles from the reconstructed slices. During the image segmentation for bubbles, we used a dynamic enhancement algorithm [29], which is incorporated in ImageJ. It allows us to set parameters of threshold of grey level enhancement, denoted as  $T$ . By choosing a value of  $T$ , the grey value of the original image will be converted the enhance data plot. According to the actual situation of the interference image, the distribution range of the grey value of the bubble area is narrow. The segmentation accuracy for air bubbles using this simple thresholding method is acceptable. The local images of a slice obtained at different step of the segmentation using thresholding method are shown in Figure 2.



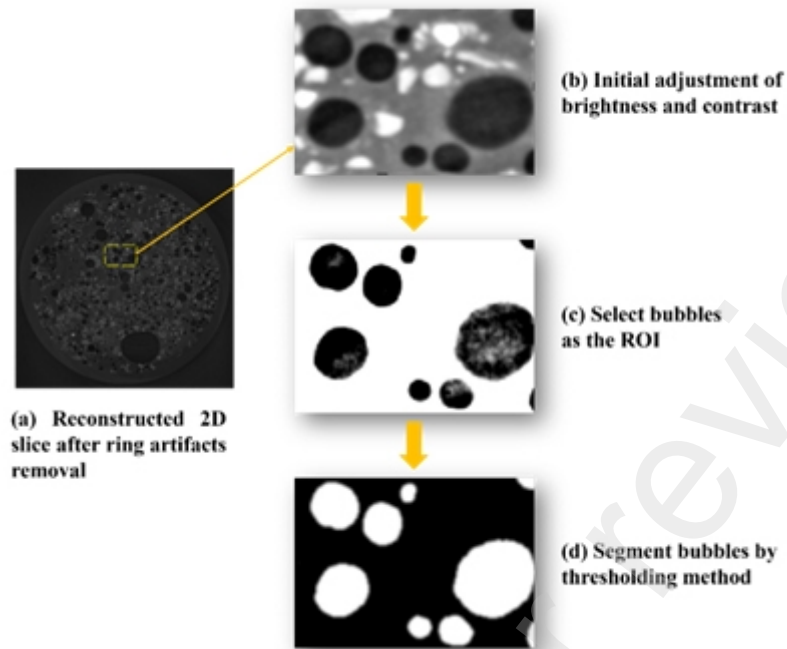


Figure 2. Flow diagram for the thresholding segmentation of bubbles in a slice.

In this bitumen froth system, particles unlike the round and uniform shape air bubbles, have irregular shapes with sharp corners and edges, making it challenging for segmentation algorithms to accurately identify and delineate their boundaries. The thresholding techniques, even with grey level enhancement, are insufficient for accurate segmentation of mineral particles. To achieve more precise minerals segmentation, we employed the watershed method [30]. It simulates the rise and flooding of water from local minima, dividing the image into regions. Thus, it can effectively separate overlapping particles by treating the image as a topographic surface, where high-intensity regions are peaks and low-intensity regions are valleys. In comparison to the thresholding method, watershed method helps in delineating individual particles even when they touch or slightly overlap. Figure 3 illustrates the obtained images by both thresholding and watershed techniques, where panel (a) shows the reconstructed original image, and (b) shows the selected particles as ROI. Panel (c) and (d) shows the segmentation results using thresholding and watershed methods, respectively. The thresholding segmentation method often merges closely positioned particles into

single clusters, as seen in the upper right corner of panel (b) and (c) in red circles. Conversely, the watershed method accurately distinguishes these particles (panel d). Although over segmentation can occur with the watershed method, as indicated by the yellow circles, it has minimal impact on our study because of the large sample size. We analyzed 100 reconstructed slices, each containing more than 1000 identified particles. A single digit number of over-segmented or under-segmented particles is negligible compared to the overall number of particles, ensuring the particle size distribution remains largely unaffected. Thus, we adopted the watershed method that provides a more robust and precise segmentation for mineral particles in the bitumen froth system.

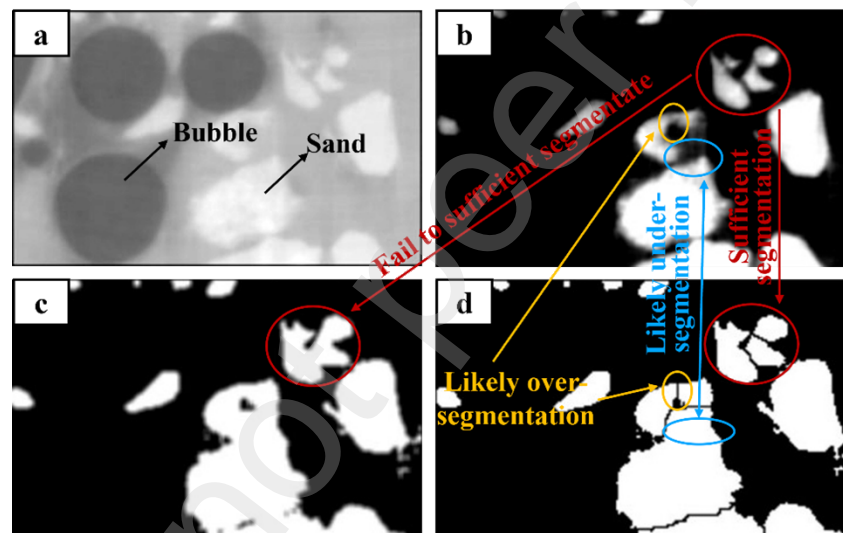


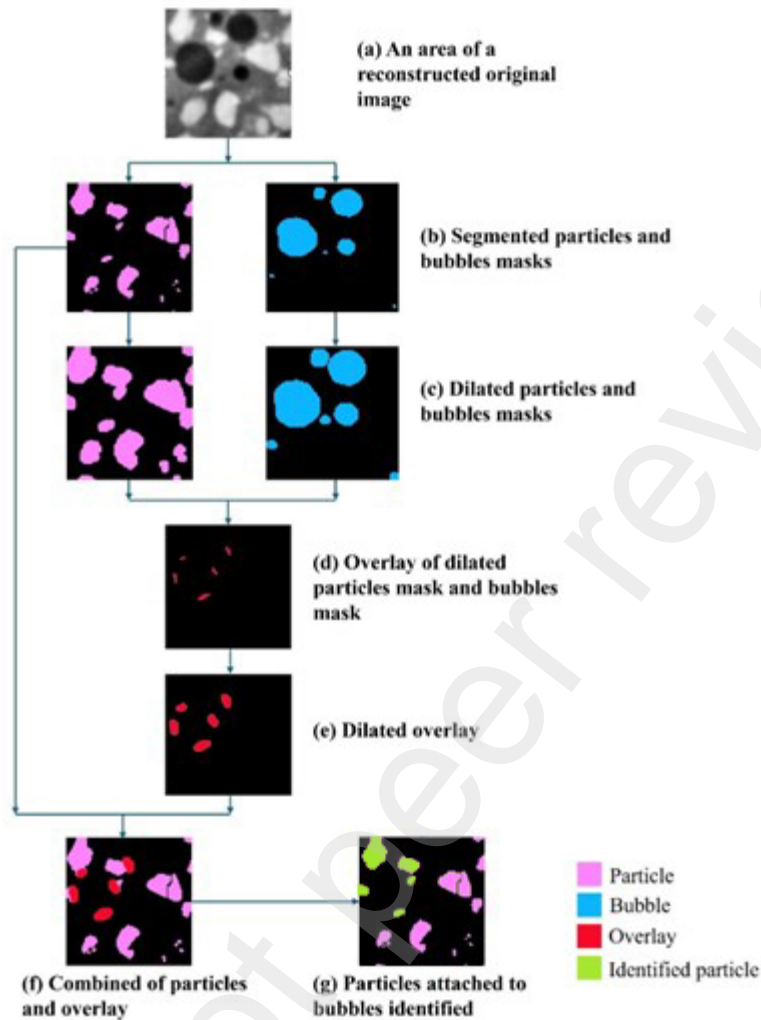
Figure 3. Images of a local area for (a) reconstructed original image, (b) binary mask with particles selected, (c) particles segmented by thresholding method, and (d) particles segmented by watershed method.

In froth flotation, particles attached to air bubbles are considered to be brought directly to the froth layer through true flotation. The composition and content of these particles are important characterization in flotation [31]. To statistically analyze the particles attached to the air bubbles,

our work innovatively segmented the overlay between particles and bubbles. The detailed image segmentation procedures are as follows (Figure 4):

- 1) the reconstructed image (panel a) was segmented to isolate particles and bubbles using the previously mentioned methods, resulting in the regions of ROIs shown in panel (b).
- 2) Each segmented particle and bubble were then dilated by two pixels to generate the updated ROIs, as shown in panel (c). The ROIs were assigned a value of 1, and the background was set to 0.
- 3) The overlay area of the dilated bubbles and particles were segmented using the “AND” function of ImageJ, producing an “overlay” image shown in panel (d).
- 4) The overlay was further dilated by two pixels (panel e), and we then combine this dilated overlay with the original, non-dilated particles mask to obtain a combined mask (panel f).
- 5) The combined mask was then segmented using the thresholding method, the particles with air bubble attached or not attached are differentiated as shown in panel (g).

This method accurately counted the particles attached to bubbles (i.e., those carried over to the froth layer due to true flotation attaching to air bubbles). Following segmentation, the area of each selected particle was extracted for further quantitative analysis.



188

189 Figure 4. Image processing procedure for identifying particles attached to bubbles. The original  
 190 images are all grayscale, the colors here are just for distinguishing the different components more  
 191 easily.

192 The 3D model of the bitumen froth was created using Avizo software developed by Thermo Fisher  
 193 Scientific. The stack of 100 slices binary masks was imported, and an ortho slice linked to the  
 194 mask was then created for visualization. Figure 5 shows the 3D diagram of air bubbles, mineral  
 195 particles, and each individual entity. Each particle was labelled to obtain detailed information such  
 196 as volume. The volumes of the 3D particles were calculated by voxel counting by Avizo software.

To express their sizes, the equivalent spherical diameter was determined by calculating the diameter of a sphere with a volume equal to that of the particle. Based on the volume and equivalent diameter, characterization of the particle in the fresh bitumen froth was reported in the results and discussion section.

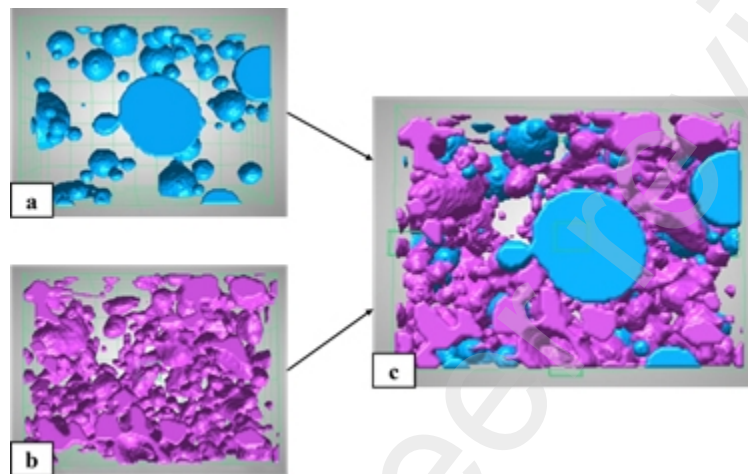


Figure 5. Diagram of 3D view of (a) air bubbles, (b) particles, and (c) each individual entity.

### 3. Results and discussion

#### 3.1 Sand and non-sand minerals

The synchrotron-based micro-CT imaging method uniquely enables in-situ visualization of the particle distribution and positions within the fresh bitumen froth. The visualization of particles within the bitumen froth provided detailed insights into the particle size distribution, overcoming the limitations of traditional off-site analysis methods. As mentioned previously, 3D model was built using the 100 reconstructed slices; the characterization of particles (sand and non-sand) results are presented in Figure 6 (a). Due to the large differences between data within the same group, the vertical axes in the charts are represented using a logarithmic scale. As can be seen, 13616 sand particles in total were detected from the 3D image, whereas only 618 non-sand

particles (i.e., heavy minerals) were segmented. This indicate that sand particles constitute the majority, making up 95.66% of the total particle count (i.e., both sand and non-sand particles). The total volume of sand particles is  $5.898 \times 10^9 \mu\text{m}^3$ ; and the total volume of non-sand particles is significantly lower at  $0.040 \times 10^9 \mu\text{m}^3$ . According to the characterization of heavy minerals in Athabasca oil sands ore [32], the heavy minerals are primarily rutile ( $\text{TiO}_2$ ) and zircon ( $\text{ZrO}_2$ ), with average content of approximately 0.35 wt.% for  $\text{TiO}_2$  and 0.032 wt.% for  $\text{ZrO}_2$  [33]. Assuming a specific density of 2.68 for sand particles and treating non-sand minerals as  $\text{TiO}_2$  with a specific density of 4.23, the mass percentage calculated based on the volume of percentage was 98.9 wt.% for sand and 1.1 wt.% for non-sand minerals. This closely matches the referenced mineralogical analysis for Athabasca bitumen froth [34], which reported a mass pull of 4 wt.% solids from the oil sands ore and a  $\text{TiO}_2$  content concentrated to about 6 wt.%. This indicates that approximately 70 wt.% of all the  $\text{TiO}_2$  in the ore has been extracted into the froth. In our flotation test, the mass pull was about 18 wt.% of solids. Assuming we also extracted 70 wt.% of the  $\text{TiO}_2$ , the  $\text{TiO}_2$  content in the bitumen froth should be 1.36 wt.%.  $\text{TiO}_2$  carrier minerals in the bitumen froth are typically small, with about 6-7 wt.% being less than  $2 \mu\text{m}$  [34]. Given that the resolution of our micro-CT images is  $6.5 \mu\text{m}$  per pixel, some  $\text{TiO}_2$  cannot be detected. This explains why the analyzed result (1.1 wt.%) from the 3D image is slightly lower than the estimated result (1.36 wt.%). An X-ray detector with higher resolution ( $2 \mu\text{m}$ ) will be used in our next report in this series to achieve a more accurate result for more complex analysis.

Figure 6 (b) shows the particles characterization results obtained from slices, where the particles amount was counted from all the 100 slices and the particles area was the average for per slices. In total, 146,265 sand particles were detected, covering a total of area of  $3,662,695 \mu\text{m}^2$  per slice. In addition, 3,657 non-sand particles were segmented, accounted for about 2.45% of total number

of all particles. The non-sand particles covering an area of 62,330  $\mu\text{m}^2$  per slice, making up about 1.67% of the area for all particles. Non-sand particles, which make up 2.45% of the total number, occupy only 1.67% of the area.

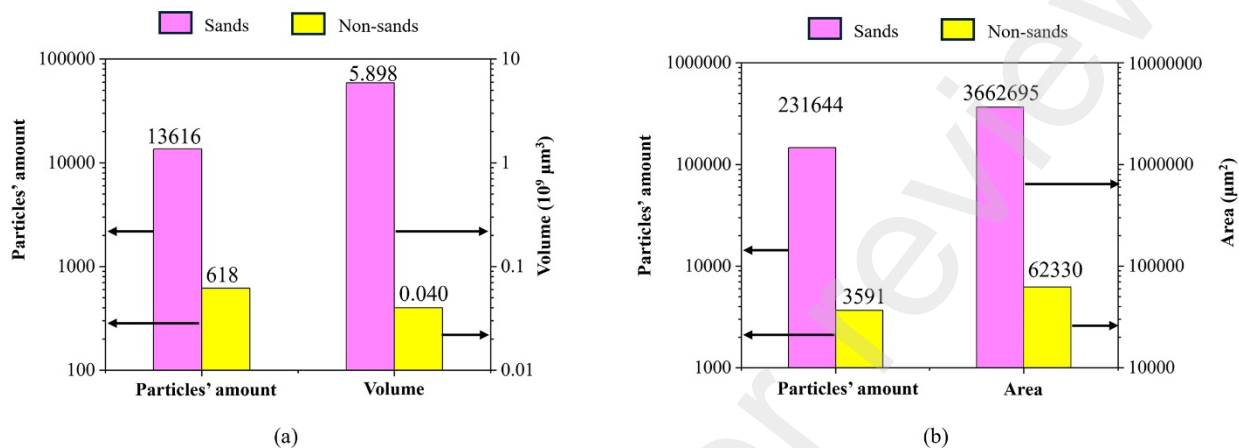


Figure 6. The amount and occupied volume/area of sand and non-sand particles analyzed from (a) 3D model, and (b) reconstructed slices displayed in semilogarithmic chart.

Table 1 provides a comparison of the particle size distribution for sand and non-sand particles, as measured in both reconstructed slices and 3D model stacked from these slices. In the slices data, sand particles have a median particle size (P50) of 42.1  $\mu\text{m}$ , while non-sand particles exhibit a median particle size of 33.1  $\mu\text{m}$ . This trend is consistent across other percentiles, with sand particles showing larger sizes compared to non-sand particles. Similarly, in the data for 3D model, sand particles have a median particle size of 42.8  $\mu\text{m}$ , whereas non-sand particles have a median particle size of 30.7  $\mu\text{m}$ . The P80 and P20 values also confirm that non-sand particles are consistently smaller than sand particles in both slices and 3D measurements. Given the 6.5  $\mu\text{m}$  detector resolution, the results from slices and 3D data are generally consistent, except for the P80 value of sand particles. Specifically, the P80 value for sand particles is 68.8  $\mu\text{m}$  in slices data and 87.3  $\mu\text{m}$  in 3D data. This difference is likely due to over-segmentation of larger particles in the

slices data when using the watershed segmentation method. Overall, the analysis clearly indicates that non-sand particles are smaller than sand particles. The consistency between the slices and 3D data confirms slices quantification also can provide the reliable results, particularly when analyzing the particles with medium or small size. These findings underscore the capability of the CT method, coupled with advanced image processing techniques, to provide real-time and highly accurate particle quantification results. The synchrotron-based micro-CT imaging not only visualizes the internal structure of bitumen froth but also offers precise and reliable data that aligns with traditional off-site analytical methods.

Table 1. The particle size distribution of sand and non-sand minerals analyzed from the reconstructed slices and their stacked 3D model.

| Images   | Particle type | Particle size distribution ( $\mu\text{m}$ ) |      |      |
|----------|---------------|----------------------------------------------|------|------|
|          |               | P80                                          | P50  | P20  |
| Slices   | Sand          | 68.8                                         | 42.1 | 24.3 |
|          | Non-sand      | 55.1                                         | 33.1 | 18.5 |
| 3D model | Sand          | 87.3                                         | 42.8 | 19.9 |
|          | Non-sand      | 50.8                                         | 30.7 | 17.4 |

### 3.2 Particles attaching to air bubbles

As mentioned previously, we developed an innovative image transformation technique, successfully identified particles attaching to air bubbles as shown in Figure 4. From the reconstructed slices, we quantified the particle size distribution of particles attaching to bubbles and those not attaching to air bubbles. The amount and covered area of particles that attaching to bubbles are summarized in Figure 7. In the analysis of sand particles attached to bubbles, 44,318 sand particles out of 146,265 (30.3% of the total sand particles) were found attached to bubbles, covering an area of 1,955,879  $\mu\text{m}^2$  (53.4% of the total area occupied by sand particles). Particles attached to bubbles make up 30.3% of the total count but occupy more than half of the total area



(53.4%). This suggests that the average size of the particles attached to bubbles is larger than that of the free particles not attached to bubbles. Additionally, the particles not attached to bubbles, despite being more numerous, covering less area, indicating they were predominantly consisting of smaller particles. Similarly, for the non-sand particles, 434 particles (11.8%) were attached to bubbles, covering an area of 18,325  $\mu\text{m}^2$  (29.4% of the total non-sand particle area). It should be noted that particles of the same type of mineral have the same density, so the proportion of the area occupied by particles attached to bubbles to the total particle area also represents the proportion of the mass of particles attached to bubbles to the total particle mass. This finding highlight that a significant portion of sands carried over to the bitumen froth are associated with air bubbles. Such detailed spatial information cannot be observed through other methods.

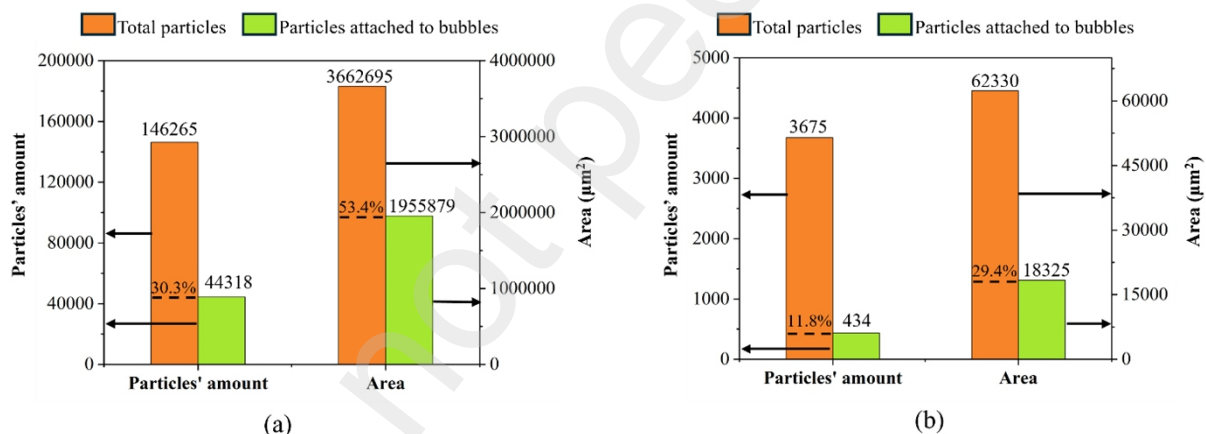


Figure 7. The amount and covered area of total particles and particles attached to bubbles for (a) sand, and (b) non-sand minerals.

It is very interesting to dig deeper based on the quantitative analysis of particles at two different positions: attaching to or not attaching to air bubbles. The particle size distribution is revealed in Figure 8. A significant difference between sand particles attaching to air bubbles and those not attaching is observed. Specifically, the median particle size (P50) for sand particles attached to air bubbles is 67.6  $\mu\text{m}$ , whereas for those not attached, it is only 35.7  $\mu\text{m}$ . For non-sand particles, the

median size (P50) is 35.3  $\mu\text{m}$  for attached particles and 30.6  $\mu\text{m}$  for those not attached, showing  
 less variation compared to sand particles. This observation suggests fine particles were entrained  
 into the bitumen froth not associated with air bubbles. One such mechanism is slime coating, a  
 phenomenon that has been previously discussed but never directly observed until now. The current  
 study's visualization and quantitative analysis provide concrete evidence of slimes (fine particles)  
 were carried over to the froth primarily due to this effect rather than true flotation. This insight  
 highlights the importance of this study to uncover the distribution and positioning of particles in  
 the bitumen froth and which mechanisms are at work making the presence of unwanted fine  
 particles in the froth. The new knowledge generated is very important in the bitumen extraction  
 process to enhance the separation efficiency.

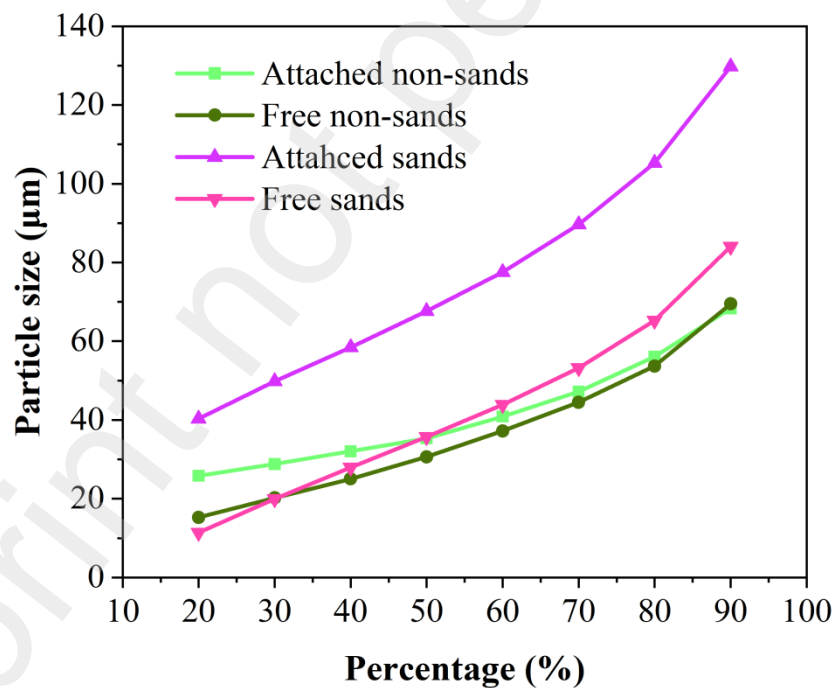


Figure 8. The particle size distribution for attached non-sand particles, free non-sand particles,  
 attached sand particles, and free sand particles.

#### 4. Conclusion

Synchrotron-based micro-CT was used to directly visualize the distribution of solid particles within the fresh bitumen froth with air bubbles. Through the analysis of 100 reconstructed slices and the 3D model built from them, we successfully segmented and quantified both sand and non-sand particles. Sand particles are predominant, making up 99.32% of the total volume. Non-sand particles, constituting only 0.68% by volume. The median particle size (P50) for sand particles is 42  $\mu\text{m}$ , with non-sand minerals smaller in size compared to sand particles. These findings are almost identical to the results obtained by traditional off-site (Dean Stark) methods, confirming the accuracy of this advanced imaging technique.

A key finding from this study is the successful identification of true flotation particles (both sands and non-sands). Particles were differentiated based on their attachment to air bubbles, achieved through our imaging, transformation and segmentation methods. Particles attached to bubbles in bitumen froth were considered to enter the froth specifically through true flotation, while the remaining particles enter the froth layer for other reasons such as entrainment by water or entrapment by bitumen. With the identification of bubbles attached particles, it was found that approximately 50 wt.% of sand particles attach to air bubbles (i.e., true flotation) and these attached particles are significantly larger compared to those that do not attach. This indicates that fine particles are carried over to the bitumen froth through entrapment by bitumen or entrainment by water, indirectly providing evidence for the existence of slime coating in bitumen water-based extraction. Our study provides an in-situ method to observe the distribution and association of particles in the froth. This approach is innovative and crucial for understanding the mechanisms behind solids carryover. The next step is finding concrete visual evidence of slime coating because the need to address slime coating is important to improve separation efficiency and reduce

unwanted fine particles in the froth. Our research work supports the development of strategies to enhance bitumen extraction processes and optimize the quality of the froth.

## **Acknowledgements**

This work was supported by the start-up funding from the Faculty of Engineering at the University of Alberta. The research described in this paper was performed at the Canadian Light Source (CLS), a national research facility of the University of Saskatchewan, which is supported by the Canada Foundation for Innovation (CFI), the Natural Sciences and Engineering Research Council (NSERC), the National Research Council (NRC), the Canadian Institutes of Health Research (CIHR), the Government of Saskatchewan, and the University of Saskatchewan. The authors are grateful for the assistance from Dr. Qi Liu and Dr. Natalia Semagina of the Department of Chemical and Materials Engineering at the University of Alberta. Additional follow-up research, which will be financially supported by the Institute for Oil Sands Innovation (project IOSI 2024-03), is currently underway. Although this research was conducted prior to the commencement of the IOSI project, the authors appreciate the funding opportunity from IOSI.

## **References**

1. Khattak MA, Yasin NS, Andjani HN, Tajuddin PN, Narajah S, Fei SZ et al. Global energy security and North America: A review. *Journal of Advanced Research in Applied Sciences and Engineering Technology*. 2018; 11(1): 82-98.
2. Isaacs E. The Canadian oil sands in the context of the global energy demand. *Horizon*. 2008; 110: 232-000.

3. Record high crude oil production largely driven by oil sands: Crude oil production year in review 2023. Available at: <https://www.statcan.gc.ca/o1/en/plus/5781-record-high-crude-oil-production-largely-driven-oil-sands-crude-oil-year-review-2023>.
4. Masliyah J, Zhou ZJ, Xu Z, Czarnecki J, Hamza H. Understanding water-based bitumen extraction from Athabasca oil sands. The Canadian Journal of Chemical Engineering. 2004 Aug; 82(4): 628-54. <https://doi.org/10.1002/cjce.5450820403>.
5. Rao F, Liu Q. Froth treatment in Athabasca oil sands bitumen recovery process: A review. Energy & fuels. 2013 Dec 19; 27(12): 7199-207. <https://doi.org/10.1021/ef4016697>.
6. Khodaei Booran S, Wang X, Tan X, Liu Q. Effect of Carbon Dioxide on Asphaltene Precipitation from Bitumen–Heptane Mixtures. Energy & Fuels. 2020 Jul 16; 34(8): 9483-91. <https://doi.org/10.1021/acs.energyfuels.0c01562>.
7. Meng, J, Microscale dynamics of dilution-induced asphaltene precipitation. 2022. <https://doi.org/10.7939/r3-ectf-z523>.
8. Zhou ZA, Li H, Chow R, Adeyinka OB, Xu Z, Masliyah J. Impact of fine solids on mined athabasca oil sands extraction II. Effect of fine solids with different surface wettability on bitumen recovery. The Canadian Journal of Chemical Engineering. 2017 Jan; 95(1): 120-6. <https://doi.org/10.1002/cjce.22564>.
9. Li A, Xu Z. Determination of clay content in Canadian oil sands using x-ray florescence spectroscopy for diagnosis of ore processability. The Canadian Journal of Chemical Engineering. 2020 Jan; 98(1): 360-72. <https://doi.org/10.1002/cjce.23599>.
10. Ata S. The detachment of particles from coalescing bubble pairs. Journal of colloid and interface science. 2009 Oct 15; 338(2): 558-65. <https://doi.org/10.1016/j.jcis.2009.07.003>.

- 371 11. Dracos T. Particle tracking velocimetry (PTV) basic concepts. In: Three-Dimensional  
372 Velocity and Vorticity Measuring and Image Analysis Techniques: Lecture Notes from the  
373 Short Course held in Zürich, Switzerland, 3–6 September 1996 (pp. 155-160). Dordrecht:  
374 Springer Netherlands.
- 375 12. Tropea C, Yarin AL, Foss JF, editors. Springer handbook of experimental fluid mechanics.  
376 Berlin: Springer; 2007 Oct 9.
- 377 13. Raffel M, Willert CE, Scarano F, Kähler CJ, Wereley ST, Kompenhans J. Particle image  
378 velocimetry: a practical guide. springer; 2018 Apr 3.
- 379 14. Estevadeordal J, Goss L. PIV with LED: particle shadow velocimetry (PSV) technique. In:  
380 43rd AIAA aerospace sciences meeting and exhibit 2005 Jan 10 (p. 37).  
381 <https://doi.org/10.2514/6.2005-37>.
- 382 15. Solórzano E, Pardo-Alonso S, De Saja JA, Rodríguez-Pérez MA. Study of aqueous foams  
383 evolution by means of X-ray radioscopy. Colloids and Surfaces A: Physicochemical and  
384 Engineering Aspects. 2013 Dec 5; 438: 159-66.  
385 <https://doi.org/10.1016/j.colsurfa.2013.01.052>.
- 386 16. Mathews JP, Campbell QP, Xu H, Halleck P. A review of the application of X-ray  
387 computed tomography to the study of coal. Fuel. 2017 Dec 1; 209: 10-24.  
388 <https://doi.org/10.1016/j.fuel.2017.07.079>.
- 389 17. Anzoom SJ, Bournival G, Ata S. Micro-CT imaging of a frozen bubble cluster: Sample  
390 holder development and image processing techniques. Separation and Purification  
391 Technology. 2024 May 5; 335: 126111. <https://doi.org/10.1016/j.seppur.2023.126111>.
- 392 18. Ghorbani Y, Becker M, Petersen J, Morar SH, Mainza A, Franzidis JP. Use of X-ray  
393 computed tomography to investigate crack distribution and mineral dissemination in

sphalerite ore particles. Minerals Engineering. 2011 Oct 1; 24(12): 1249-57.  
<https://doi.org/10.1016/j.mineng.2011.04.008>.

19. Chen X, Verma R, Espinoza DN, Prodanović M. Pore-scale determination of gas relative permeability in hydrate-bearing sediments using X-ray computed micro-tomography and lattice Boltzmann method. Water Resources Research. 2018 Jan; 54(1): 600-8.  
<https://doi.org/10.1002/2017WR021851>.

20. Miller JD, Lin CL, Hupka L, Al-Wakeel MI. Liberation-limited grade/recovery curves from X-ray micro CT analysis of feed material for the evaluation of separation efficiency. International Journal of Mineral Processing. 2009 Sep 1; 93(1): 48-53.  
<https://doi.org/10.1016/j.minpro.2009.05.009>.

21. Tang F, Wu Z, Yang C, Osenberg M, Hilger A, Dong K et al. Synchrotron X-ray tomography for rechargeable battery research: fundamentals, setups and applications. Small Methods. 2021 Sep; 5(9): 2100557.  
<https://doi.org/10.1002/smtd.202100557>.

22. García-Moreno F, Kamm PH, Neu T, Heim K, Rack A, Banhart J. In situ X-ray tomography of aqueous foams: Analysis of columnar foam generation. Colloids and Surfaces A: Physicochemical and Engineering Aspects. 2017 Dec 5; 534: 78-84.  
<https://doi.org/10.1016/j.colsurfa.2017.03.011>.

23. Kamm PH, García-Moreno F, Neu TR, Heim K, Mokso R, Banhart J. Fast Synchrotron X-Ray Tomography of Dynamic Processes in Liquid Aluminium Alloy Foam. Advanced Engineering Materials. 2017 Nov; 19(11): 1600550.  
<https://doi.org/10.1002/adem.201600550>.

24. Wysokinski TW, Chapman D, Adams G, Renier M, Suortti P, Thomlinson W. Beamlines of the biomedical imaging and therapy facility at the Canadian Light Source-Part 2. InJournal of Physics: Conference Series 2013 Mar 22 (Vol. 425, No. 7, p. 072013). IOP Publishing.25. Fitzgerald, R., *Phase-sensitive x-ray imaging*. Physics today, 2000. **53**(7): p. 23-26. <https://doi.org/10.1088/1742-6596/425/7/072013>.
26. Faragó T, Gasilov S, Emslie I, Zuber M, Helfen L, Vogelgesang M, Baumbach T. Tofu: A fast, versatile and user-friendly image processing toolkit for computed tomography. Journal of Synchrotron Radiation. 2022 May 1; 29(3): 916-27. <https://doi.org/10.1107/S160057752200282X>.
27. Wei Z, Wiebe S, Chapman D. Ring artifacts removal from synchrotron CT image slices. Journal of Instrumentation. 2013 Jun 17; 8(06): C06006. <https://doi.org/10.1088/1748-0221/8/06/C06006>.
28. Marr D, Hildreth E. Theory of edge detection. Proceedings of the Royal Society of London. Series B. Biological Sciences. 1980 Feb 29; 207(1167): 187-217. <https://doi.org/10.1098/rspb.1980.0020>.
29. Kohler R. A segmentation system based on thresholding. Computer Graphics and Image Processing. 1981 Apr 1; 15(4): 319-38. [https://doi.org/10.1016/S0146-664X\(81\)80015-9](https://doi.org/10.1016/S0146-664X(81)80015-9).
30. Seal A, Das A, Sen P. Watershed: an image segmentation approach. International Journal of Computer Science and Information Technologies. 2015; 6(3): 2295-7.
31. Ross VE. Particle-bubble attachment in flotation froths. Minerals Engineering. 1997 Jul 1; 10(7): 695-706. [https://doi.org/10.1016/S0892-6875\(97\)00049-6](https://doi.org/10.1016/S0892-6875(97)00049-6).
32. Liu Q, Cui Z, Etsell TH. Characterization of Athabasca oil sands froth treatment tailings for heavy mineral recovery. Fuel. 2006 Mar 1; 85(5-6): 807-14.



- 439 <https://doi.org/10.1016/j.fuel.2005.08.032>.
- 440 33. McCosh R. Geology executive summary from mineral development agreement. Final  
441 report, Alberta chamber of resources. 1996.
- 442 34. Kaminsky HA. Characterization of an Athabasca oil sand ore and process streams. 2008.  
443 <https://doi.org/10.7939/r3-60y0-hk65>.
- 444